Apparatus for combined nanoscale gravimetric, stress, and thermal measurements

Joseph B. Murray,[1,a)] Kevin J. Palm,[1,2] Tarun C. Narayan,[1] David K. Fork,[3] Seid Sadat,[3] and Jeremy N. Munday[1,4,a)]

[1]*Institute for Research in Electronics and Applied Physics, University of Maryland, College Park, Maryland 20742, USA*

[2]*Department of Physics, University of Maryland, College Park, Maryland 20742, USA*

[3]*Google, Inc., 1600 Amphitheatre Parkway, Mountain View, California 94043, USA*

[4]*Department of Electrical and Computer Engineering, University of Maryland, College Park, Maryland 20742, USA*

We present an apparatus that allows for the simultaneous measurement of mass change, heat evolution, and stress of thin film samples deposited on quartz crystal microbalances (QCMs). We show device operation at $24.85 \pm 0.05\,^\circ$C under 9.31 ± 0.02 bars of H_2 as a reactive gas. Using a 335 nm palladium film, we demonstrate that our apparatus quantifies curvature changes of 0.001 m^{-1}. Using the QCM curvature to account for stress induced frequency changes, we demonstrate the measurement of mass changes of 13 ng/cm^2 in material systems exhibiting large stress fluctuations. We use a one-state nonlinear lumped element model to describe our system with thermal potentials measured at discrete positions by three resistance temperature devices lithographically printed on the QCM. By inputting known heat amounts through lithographically defined Cr/Al wires, we demonstrate a 150 μW calorimetric accuracy and 20 μW minimum detectable power. The capabilities of this instrument will allow for a more complete characterization of reactions occurring in nanoscale systems, such as the effects of hydrogenation in various metal films and nanostructures, as well as allow for direct stress compensation in QCM measurements. *Published by AIP Publishing.* https://doi.org/10.1063/1.5040503

INTRODUCTION

Chemistry in nanoscale systems is increasingly important in a wide variety of fields from energy and information storage to catalysis and sensing.[1–8] The shift away from the macroscale allows for dimensional reduction and dramatic changes in surface-to-volume ratios, which in-turn present opportunities to tailor the thermodynamics and kinetics. Despite the small amount of material present in a nanoscale system, reactions can still produce significant amounts of heat and stress that can change the chemical and physical properties of the material. As such, it is crucial to quantify the mechanical, optical, and thermal properties of these systems to inform the design of devices exploiting these chemical processes.

Quartz crystal microbalances (QCMs) are commonly used to observe nanoscale chemical reactions. A QCM is a quartz wafer (typically a disc) with its crystal orientation cut to produce a shear displacement in the presence of an electric field normal to its face. Applying an oscillating electric field between two electrodes on opposite sides of the QCM excites a shear wave in the quartz disc due to its piezoelectric response. The resonance frequency of this oscillation is very sensitive to the material attached to the surface of the resonator, which causes a change in the acoustic impedance of that interface. This frequency changes (very nearly) linearly with added rigid mass, such as a thin metal film, and thus can be used to detect changes of mass due to chemical or physical processes.[9,10] This mass sensitivity lends itself to a number of applications as far reaching as protein sensing and electrochemical degradation.[11]

The QCM resonance frequency also has a pronounced dependence on a number of other parameters including pressure, density, and viscosity of the medium surrounding the QCM, temperature, and stress (e.g., from mounting or from stress in an adhered thin film).[12–14] In order to compensate for these myriad effects when performing a mass measurement, it is necessary to couple multiple measurement techniques to independently determine the other parameters to which the QCM is sensitive. Doing so, however, not only results in a more accurate determination of the mass change (e.g., by accounting for stress effects) but also simultaneously provides greater understanding of a chemical or physical process than a QCM measurement alone could (e.g., by leveraging knowledge of sample stresses). As such, QCM samples can be integrated into a modular experimental apparatus to correctly determine not only mass changes but also a range of complementary processes in a chemical reaction.

Our system combines the QCM platform in a pressure and temperature controlled environmental chamber with optical access, which allows *in situ*, high-speed, stress measurements to properly characterize mass change. It also includes optical, calorimetric, and electrical measurements for a more complete picture of chemical reactions on nanoscale structures. Here we capitalize on the planar nature of these devices to be used as interferometric mirrors (for measurement of stress by means of sample curvature) as well as substrates for

a)Authors to whom correspondence should be addressed: jnmunday@umd.edu and jmurray6@umd.edu

photolithographically defined resistance temperature devices (RTDs) that can be used for sensing or introducing known amounts of heat for calorimetry modeling. All of these measurements are made in a temperature controlled, variable pressure reaction chamber. Below, we describe the components of this system and demonstrate the system's stability and precision. We then apply this apparatus to a palladium hydrogenation reaction as an example of operation.

BACKGROUND

Each of the disparate measurement capabilities is motivated by the need to form a complete picture of nanoscale chemical reactions. The particular choices of techniques are driven by constraints of integration into our system. Below we provide background and context for these individual measurements.

Stress measurement

In some of the earliest studies measuring film stress on QCMs, EerNisse showed that quartz wafers cut along different crystal axes have significantly different relationships between the resonance frequency and film stress.[15,16] A measurement of the frequency changes on differently cut quartz wafers during hydrogenation of a palladium film deposited on the QCM, assuming the same hydrogen absorption, thickness, and stress level in both films, yielded a change in both the stress and mass associated with the reaction. However, preparing two identical films is complicated by the fact that samples grown at slightly different locations within an evaporator or with slightly different currents by electrochemical means could result in variations of film thickness and defect density. Furthermore, mass and stress do not necessarily scale linearly with the sample thickness, as thermodynamic and kinetic properties often change at small length scales. Thus, in our system, we perform simultaneous mass, stress, and thermal measurements on a single sample to control for sample-to-sample variation.

Measurements of stress not only allow for corrections in QCM measurements but can also yield significant insight into material systems beyond quantification of mass changes. For example, a combined stress and optical transmittance study on the hydrogenation of 10 nm palladium films on glass slide substrates revealed a gradual removal of a surface oxide layer that is often not evident in studies of hydrogen content in palladium.[17] A curvature measurement of electrochemical lithiation of silicon has shown that the chemical potential of lithium in silicon is heavily governed by the stress present in the material;[18] the joint measurement scheme also clearly delineates the extent to which the reaction can proceed before the film undergoes plastic deformation, which can inform further engineering of the Li/Si system.

Optical properties measurement

A number of studies have been conducted that combine optical measurement techniques with a QCM to extract unique insights into a system, surpassing what either technique could provide individually. Many of these studies focus on nanostructured samples that have a plasmonic response that depends on chemical reactivity within the environment. For example, a study of the corrosion of copper and aluminum nanoparticles was able to distinguish between two primary oxidative corrosion mechanisms.[19,20] Taken separately, neither the optical nor the QCM measurements could have distinguished between the different processes. By allowing optical access to the sample, our apparatus retains the ability to distinguish these processes.

Calorimetry

The most sensitive QCM-based calorimetry relies on heat conduction calorimetry.[21] This technique detects heat using a thermopile that is thermally grounded on one side. The generated heat flows through the thermoelectric plate creating a voltage by the Seebeck effect. This calorimeter has been shown to accurately measure heat from thin film reactions. The main drawback is that heat arising from different locations on a sample is treated equally. As such, it is challenging to distinguish between local and global events. Local photochemical processes occurring upon laser illumination can have heat conduction pathways that differ from those that homogeneously arise from the film, complicating the calorimetric analysis. Thus in our apparatus, we chose to perform calorimetry with multiple RTDs in order to allow for the localization heat effects, as opposed to the global heat conduction calorimetry. Optical calorimetry is another way to achieve this localized measurement,[22] but due to its low resolution of approximately 1 K and its dependence on a multitude of environmental factors (e.g., not only the refractive index changes but the size, shape, environment, etc. also change), we found that the RTDs were a superior measurement scheme in this context.

INSTRUMENT DESIGN AND DESCRIPTION

Table I outlines our system specifications. Our instrument design allows us to perform on-chip calorimetry with QCM substrates in order to simultaneously resolve changes in a curvature of 0.001 m^{-1} (corresponding to a stress of 0.006 MPa per micron of film thickness), changes in mass of 13 ng/cm^2, and changes in optical reflectivity of 0.3%, as well as the measurement of heat with 150 μW accuracy. This system has pressure capabilities up to 9.3 bars and a temperature range of 15–35 °C with stabilities of ±0.02 bar and ±0.05 °C, respectively. Our approach compensates for sample to sample variation by performing gravimetric, stress, and thermal measurements simultaneously on a single QCM. Calorimetry is achieved by modeling the outputs of lithographically printed Cr/Al RTDs on the sample substrate. We use sample curvature, measured by an interferometer integrated into our microscope, to measure in-plane stress. This noncontact method allows for accurate mass measurements by accounting for frequency changes due to stress effects. The optical access also allows for an external optical source such as a laser, ellipsometer, or spectrometer to be incorporated into the system. Figure 1 shows the system overview of our apparatus. Below we describe, in turn, each of the subsystems: environmental control, optical excitation, interferometry, mass measurement, and calorimetry.

TABLE I. Apparatus specifications.

Parameter	Characteristic values
Typical steady state minimum detectable power[a] (μW)	20
Measured power accuracy[b] (μW)	150
Approximate minimum detectable temperature change in the film[a] (mK)	~1
Minimum detectable concentration of H	~0.1 H/M in a 5 nm film
Operation temperature (°C)	15–35
Temperature stability	50 mK over 1 h 150 mK over 24 h
Differential temperature stability[c] (mK)	~4
Operating pressure (can reach 40 atm without optical access) (atm)	1–10
Illumination wavelength range (nm)	250–26 000
Minimum detectable Δ (curvature) (m^{-1})	0.001
Stress sensitivity	0.006 MPa per micron of film thickness
Optical excitation laser wavelength (nm)	660
Typical absorbed laser power (mW)	1-8
Optical excitation laser repetition rate (Hz)	100–500 000

[a]Defined as the RMS noise about the mean.
[b]Accuracy is defined as the power equivalent to the typical 10 h drift of RTDs.
[c]Based on the typical temperature coefficients. Calorimetry is performed without reference to a temperature.

The reactions occur in an environmental chamber capable of achieving and maintaining pressures up to 9.3 bars. The sample substrates are 25.4 mm diameter, 5 MHz polished Cr/Au QCMs (Maxtek®). The piezoelectric resonant frequency of the
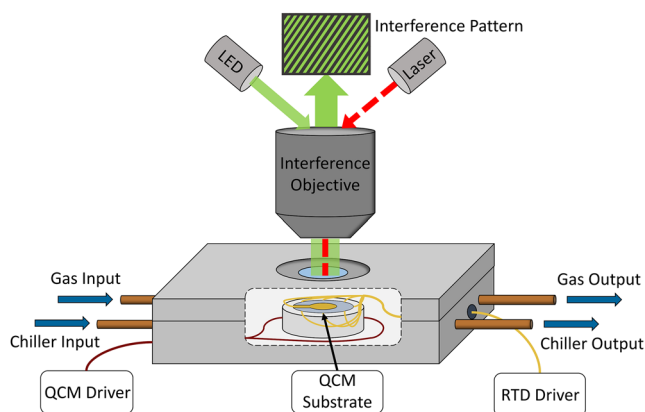

FIG. 1. System overview: The samples are deposited onto a QCM substrate. This QCM sits in an environmental chamber that controls the pressure, temperature, and gas composition. The QCM also has RTDs deposited on its surface that are electrically driven, and the reflective top surface of the QCM is used as a mirror in an adapted Michelson-Morley interferometer with a bandpass filtered LED used as a partially coherent source (see Fig. 4 for further details). The created interference pattern is used to calculate the curvature of the sample. This setup allows for the introduction of outside optical sources, such as the 660 nm diode laser depicted here. Note that the actual chamber incorporates an additional reference QCM, which we have excluded in this image for clarity (see Fig. 2).

QCM is measured by a QCM driver (Stanford Research Systems Model QCM200) using a 10 MHz Rb frequency standard (Stanford Research Systems SIM940). In our system, samples consist of either a 12.7 mm-diameter film or a nanoparticle array of the same area deposited on the center of the QCM. Samples are mounted on custom machined Macor® stages with electrodeposited Au contacts to make electrical connection with the QCM. A custom circular array of clip springs (Ted Pella 16399) is used to clamp the sample to the stage and provide *in situ* electrical contacts for devices such as RTDs. The springs are brought into contact with a custom designed flexible printed circuit board that is fed through a tube, which is hermetically sealed with epoxy (3M Scotch-Weld DP125 Translucent). Figure 2 depicts the full environmental chamber. The sample under investigation is placed on one of the stages, while a QCM without the active film is mounted on the second stage. This blank QCM allows for any ambient effects in the chamber, such as vibrations or environmental changes, to be calibrated out from the active sample data.

Figure 3 outlines the gas flow system of the apparatus. The gas flows into the system through ¼″ high pressure nylon tubing (McMaster-Carr 5173K43) with high pressure fittings (Swagelok Ultra-Torr™) to minimize leaks. The chamber is kept gas-tight with a Buna-N O-Ring. For an experiment, the flow rate of the Ar gas is regulated with a mass flow controller (MFC) (Alicat MC Series) and the reactive gases are controlled by high pressure MFCs (Bronkhorst EF-Flow Select). The Alicat MFC can operate at pressures up to 10 bars, so we choose to run experiments at slightly lower pressures to avoid damaging the unit. The 3 MFCs combine into a single gas line and are run through a heat exchanger (see Appendix B of the supplementary material) that is temperature controlled with an Oasis Three thermoelectric chiller (Solid State Cooling Systems 10-12684-1C). This chiller also regulates the temperature of the chamber by flowing water through copper pipes embedded in the chamber, as shown in Fig. 2. The gas is fed directly into the chamber from the heat exchanger through insulated tubing (Fig. S4 of the supplementary material).
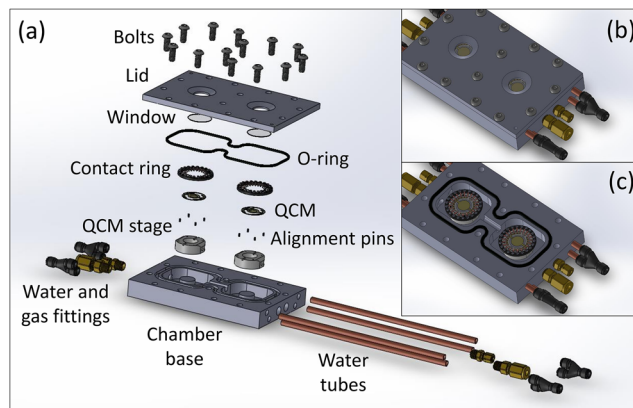

FIG. 2. (a) Exploded schematic of the environmental pressure chamber. The QCM samples are centered on a Macor stage with Teflon pins and held in place with a circular spring array. A Buna-N O-Ring provides the gas seal for the chamber. The glass window, serving as the optical port, is affixed to the chamber lid with epoxy, creating a hermetic seal. Gas, fluid, and wire feedthroughs are on the sides of the chamber. (b) Lid on and (c) lid off schematic images of the assembled sample chamber.
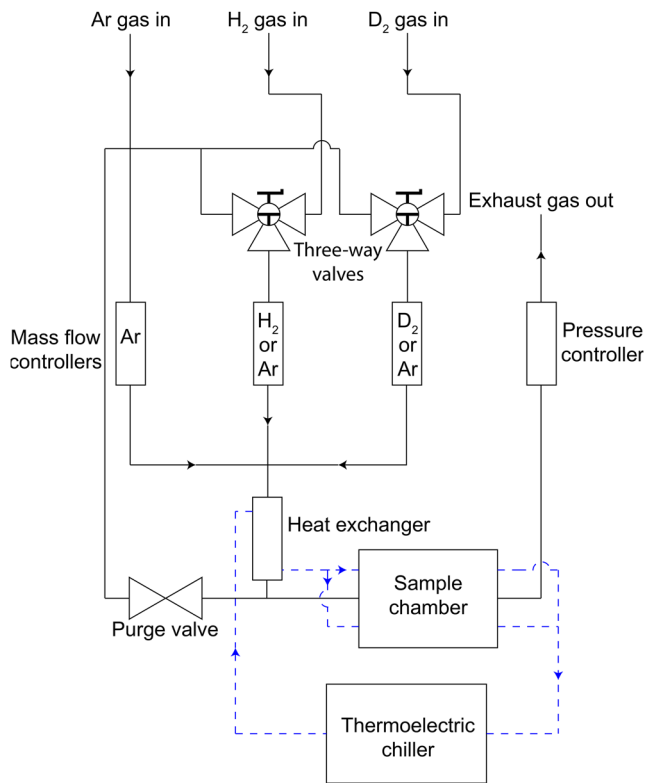
FIG. 3. Instrument gas flow system: Black lines represent the gas flow with dashed blue lines representing the water flow from the thermoelectric chiller.

The pressure is regulated with a digital pressure controller (Bronkhorst P-702CV-21KA-AAD-22V). The temperature is monitored with a thermistor (Omega ON-402-PP) embedded in the bottom of the chamber, which is read out with a digital panel meter (Omega DP32PT-C24). In order to provide the option of resetting the system to an inert environment, a set of valves allow purging of all reactive gases from the chamber and gas lines. During a purge, the 3 way valves (Swagelok SS-42GXS4) are switched to the Ar input, and Ar is flown through all MFCs at 20 SCCM each. The 2-way purge valve (Swagelok SS-41GS2) is opened, so Ar can flow directly to the chamber at

~200 SCCM, bypassing the MFCs, with the flow rate regulated by a precision needle valve (McMaster-Carr 45585K85).

Figure 4 depicts the optical setup of the apparatus. In our system, stress is determined using the curvature of the sample, which is monitored by measuring distortion of the interference pattern images produced using an adapted Michelson-Morley interferometer. A 520 nm LED is passed through a bandpass filter (Thorlabs, 520 ± 10 nm), fed into the microscope (Nikon Eclipse LV 100ND), and focused with a modified 5× interferometric objective (Nikon CF IC Epi Plan TI Interferometry Objective) incorporating a 50:50 beamsplitter. Half of the light is reflected off the sample with the other half directed to a flat, tiltable reference mirror. The tilt of this mirror allows the user to compensate for sample tilt, with the acceptable amount of tilt determined by the coherence length of the illumination (~2° for our light source). In this case, our filtered LED has an approximately square spectral density that results in a fringe amplitude that is roughly a sinc function of the sample height. Thus, for ease of analysis, we typically set the tilt to ~0.1°-0.25°. This setting avoids the antinodes of the fringe amplitude and results in a monotonic change in the phase of the fringe pattern which simplifies the analysis by including no points of ambiguous phase change (characterized visually by rings or crosses).

Note that the difference in the optical path length for the sample and reference beams should be significantly less than the coherence length of the illumination (~20 μm in our system). To that end, a compensating window cut from the same wafer used to form the window of the chamber is inserted in the path of the reference beam. Furthermore, the length of the reference arm is adjusted with stainless steel spacers to account for the change in the focal length introduced by the windows, ensuring that the image focus plane coincides with the interference focus plane. The beams are recombined at the beam splitter to form an interference pattern that is recorded with the microscope camera (Nikon DS-Fi2).

Our setup allows for other light sources to illuminate the QCM either for measurements of reflectivity, spectrometry, ellipsometry, or for other optical excitations of the sample. In
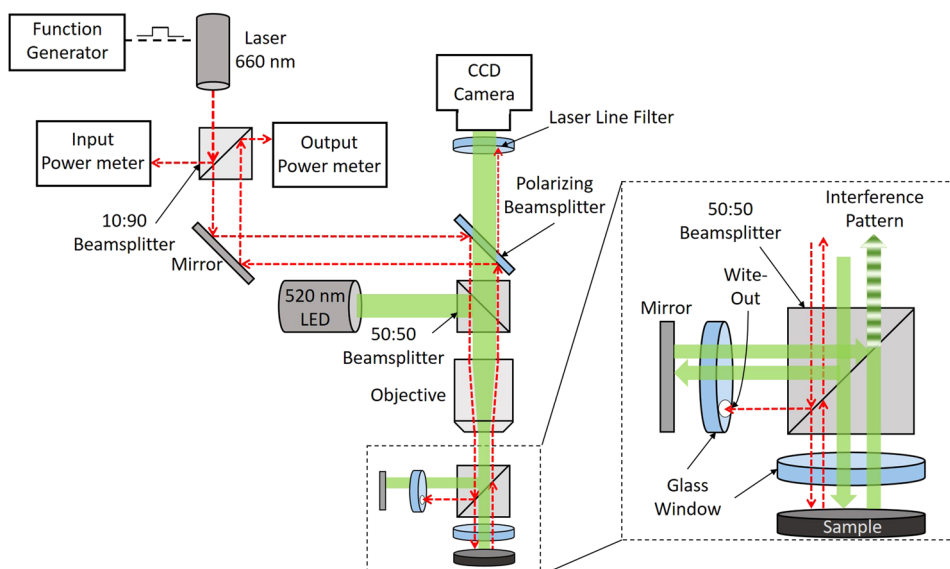

FIG. 4. Instrument optical system: Curvature measurements are obtained by collecting the interference patterns from the adapted Michelson-Morley interferometer setup with the sample acting as one of the mirrors. A 660 nm laser is fed into the system with its input and output power values recorded with optical power meters, allowing for the absorption within the sample to be calculated. The laser is blocked from entering the interference arm of the setup with a spot of Bic Wite-Out to prevent interference effects in the reflected beam.

the current apparatus, a 660 nm laser diode (Vortran Stradus 660-100) is used to illuminate the sample for optical excitation or reflectivity. The incident and reflected optical powers are recorded with Si power detectors (Edmund Optics 89-309) connected to power meters (Edmund Optics 89-307) for data collection. The laser beam is reflected onto the sample with a broadband polarizing plate beamsplitter (Edmund Optics 48-545). The section of the glass window in the interference arm intersecting the laser is blocked with a white scattering coating (Bic Wite-Out) to eliminate any interference effects of the laser. A 658 nm notch reflective filter (Thorlabs NF658-26) is placed before the camera to prevent the laser from saturating the interference image. The output of the laser is controlled with a pulse width modulation (PWM) signal from an arbitrary function generator (Tektronix AFG1062).

To perform calorimetry, heating elements and temperature measurement devices are integrated into the QCM device. For measuring temperature, three ~300 Ω Cr/Al RTDs are lithographically printed onto the QCMs, with the patterning shown in Fig. 5. The central and midway RTDs have intertwined heating elements that are used to add known quantities of heat to the localized points (i.e., the location of the RTDs) on the QCM by passing current through the elements. In addition to the RTD elements and localized heaters, the system incorporates contact pads composed of 400 nm thick Ag with a 50 nm thick Au capping layer, which connect to the sample film [see Fig. 5(d)]. These connections allow us to pass known amounts of current through the film to simulate distributed power sources such as chemical reactions. In the case of discontinuous samples, such as nanoparticle arrays, a 50 nm Cr film is deposited below the active sample to retain the capability of simulating distributed power. The electrically generated localized heat from the central heating element and the distributed heat from the film are used for calibration purposes in the calorimetry model,

as elaborated upon in the section titled Calorimetry. For a complete description of sample fabrication, see the Appendix A of the supplementary material.

The RTD sensing system driver is an Analog Devices AD7124-8 integrated circuit, implemented here via an AD7124-8 evaluation board. This driver was chosen because it met our requirements of customizability, sensitivity, noise, speed, and integrability into our custom measurement software. The AD7124-8 uses a multiplexed set of input/outputs, which can be internally connected to a differential amplifier and an analog to digital converter (ADC) or to output peripherals such as the precision variable current source in use here. See Fig. S5 of the supplementary material for a full wiring diagram. Each of the three sensing RTDs is connected in a four-point probe configuration. The voltage drop across each RTD is compared to that across a reference resistor in a ratiometric scheme, as seen in Fig. 6. We use two 470 Ω bias resistors to ensure that the inputs to the ADC meet the absolute voltage requirements (0.1 V from the rails of 0 and 3.3 V). The AD7124-8 incorporates several digital filter options, which allow the user to define the trade-off between the speed and noise. We use a sinc^4 filter with first zero at 60 Hz (primary source of noise), which results in a sampling time of 62 ms per channel. Our applications use 4 channels: 3 RTD ratiometric measurements and a voltage measurement of the reference resistor (compared to the on chip 2.5 V precision voltage source). Communication with the chip is accomplished via the SPI interface on a Teensy 3.2 development board, which also transmits data on demand with a USB COM port. The data exchange between the controlling computer and the 4 inputs takes ~270 ms for a single measurement. Our typical sampling period in the custom-built Windows user application is 350 ms; this leaves sufficient time for ~270 ms required for acquisition and 80 ms for other tasks such as saving data. The currents through the center intertwined heating element and the center disk are driven by Keithley 2450
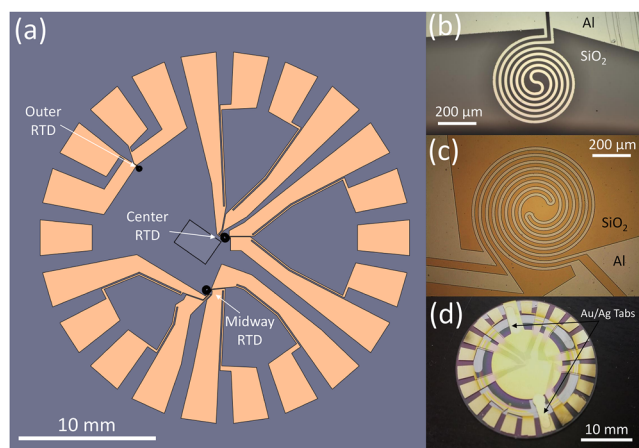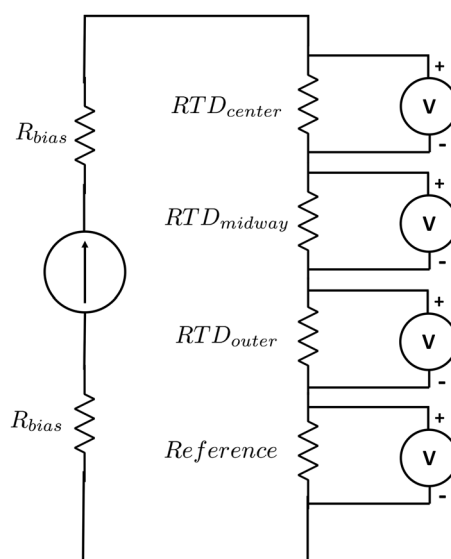

FIG. 5. (a) Mask design for samples' RTD pattern. The RTDs are located at the center of the QCM, 4 mm from the center (midway RTD), and 8 mm from the center (outer RTD). Each RTD is measured with 4-point contacts for improved accuracy. The center and midway RTDs consist of two RTDs intertwined, with one acting as a heater and the other as a sensor. The outlined box near the center of the QCM is used for consistent alignment within the microscope. (b) Outer and (c) intertwined center RTD images. (d) Sample with complete fabrication of RTDs and Ag/Au contact tabs.

FIG. 6. Schematic for the RTD current source and voltage measurement system described here. The RTD resistances are ~300 Ω, the reference resistance is 500 Ω, and the R_{bias} resistances are 470 Ω.
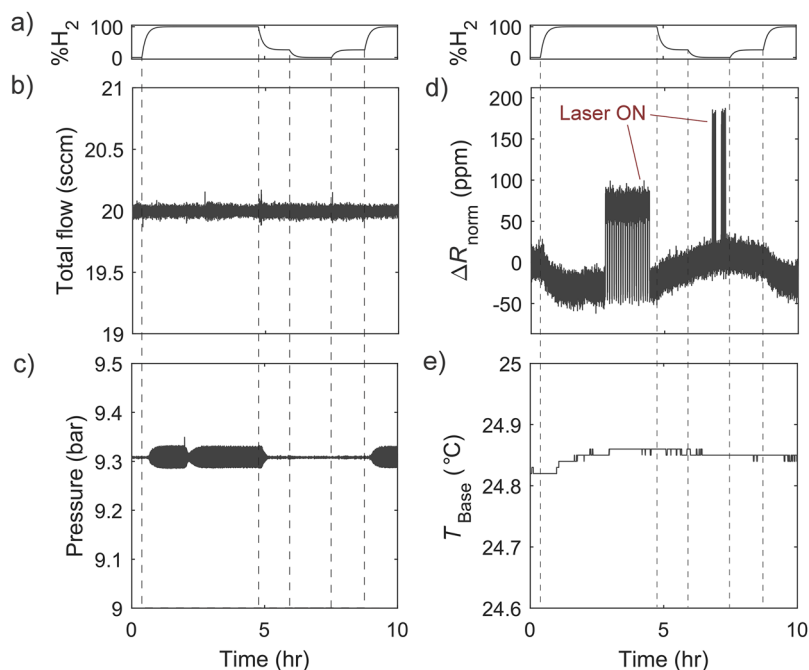
FIG. 7. Apparatus stability for a control experiment including changes in gas composition and laser excitation. Vertical dashed lines indicate a change in the H_2 flow rate set point. (a) Calculated H_2 partial pressure. (b) Total flow rate over the course of a 10 h experiment. (c) Pressure of the chamber for a fixed pressure set point. (d) Normalized differential RTD resistances through a run. The spikes in the resistances correspond to the temperature increases from the absorption of laser light. (e) Temperature of the environmental chamber, as measured by the interior thermistor.

sourcemeters in order to model known heating effects in the sample.

DEMONSTRATION OF OPERATION AND STABILITY

To demonstrate the stability of the apparatus, a control experiment was performed on a blank QCM sample with RTDs. The sample was pressurized in Ar up to 9.3 bars, switched to H_2 at 9.3 bars for 4 h, switched back to Ar for 4 h, and finally returned to H_2. During the run, the 660 nm laser was pulsed and incident on the sample while in H_2 and Ar to test how well the calorimetry model fit the heating induced by laser absorption. The data of this run are reported in Fig. 7 and show the stability of the system. The partial pressure of H_2 is not directly measured during the experiment but is calculated using the known flow rates of each of the gases, the known size of the chamber and gas lines, and the mixing coefficients of the gases. See Appendix B of the supplementary material for an example calculation. The leak rate of the system at 9.3 bars is measured to be 2 SCCM.

EXAMPLE OF STRESS AND MASS CHANGE MEASUREMENTS

The stress in the sample is characterized by the curvature of the substrate. The curvature is determined by converting the optical phase change measured by the interferometric images into a sample height change, with the process depicted in Fig. 8. The curvature is then directly converted into a corresponding frequency change that is linearly independent of the frequency change due to the mass under the thin film approximation (i.e., the film mass is much smaller than the QCM mass). First, the image is bandpass filtered and normalized so that spatial variations in image brightness and fringe sharpness are reduced. Next the image is Hilbert transformed and the phase angle of the now-complex signal is extracted. The phase angle, which varies from only 0 to 2π in a sawtooth pattern, is then unwrapped by stitching together steps in phase of 2π to produce a smooth phase surface. This phase surface can then be converted to the sample height by dividing by the phase change per change in height, $2\pi/(\lambda/2)$, where λ is the central illumination wavelength ($\lambda = 520 \pm 10$ nm for our LED). Finally,
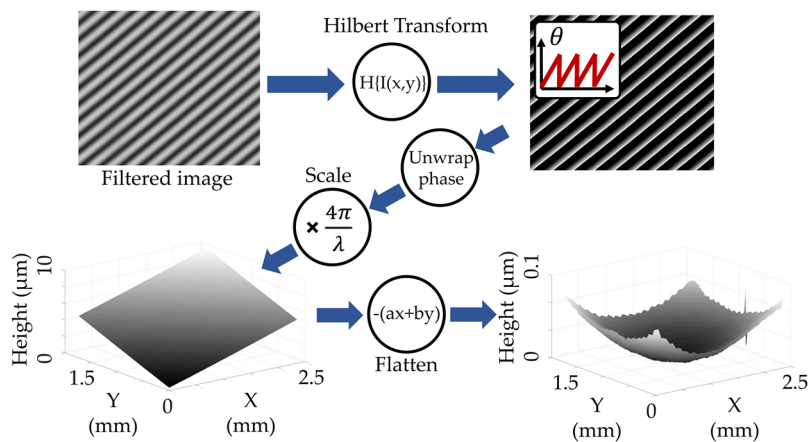

FIG. 8. Image processing flow to extract curvature measurements from the interference image. The image is filtered and normalized (Fig. S6 of the supplementary material). The instantaneous phase is then extracted from the Hilbert transform. The phase is converted to height and flattened to give the sample topography. The curvature is extracted from the second derivative of a 2D polynomial fit to the sample height.

a 2D polynomial is fit to this phase surface and the curvature can be directly extracted as the second spatial partial derivatives of the surface.

The hydrogen mass loading of the active sample is an important factor when characterizing a reaction on a film. To determine this loading, we begin with a precise measurement of the mass of the active material deposited on the sample. To accomplish this goal, we fabricate an additional, sacrificial sample that consists of a lithographically defined 1 cm × 1 cm square of the material we are characterizing on a polished Si wafer during each sample film deposition. We dissolve this film using 4 ml of either aqua regia or boiling hydrochloric acid and dilute to 100 ml as determined by film composition. We then use inductively coupled plasma atomic emission spectroscopy to determine the metal mass per area of the sample deposition. We assume that the areal mass density of the metal on the sample is the same as it is on the calibration piece (note that the areal mass density is expected to be constant even if other properties such as grain size change sample to sample), as the deposition occurs on both pieces concurrently. Knowing the area of the active film on the QCM allows us to determine the exact mass of the active material. Once the mass is known, we determine the loading in the film by subtracting the calculated frequency changes due to stress and environmental effects from the total frequency change (frequency compensation discussed below).

To calculate the contribution of stress to the frequency shift measured by the QCM, we use a combined technique of numerical and analytical calculations. We numerically calculate in COMSOL the amount of stress induced in the QCM due to curvature changes. In the simulation, we bound the system to be immobile at the edges to match our conditions of the spring ring holding down the QCM. We find the relationship between curvature and frequency change analytically by calculating the propagation speed of the shear wave through the crystal and then integrating over two times the length of the crystal to get the frequency. The final output of our derivation gives

$$\Delta f_\sigma = \alpha \Delta \kappa, \tag{1}$$

where α is the calculated curvature to frequency conversion factor equal to -777 Hz m and $\Delta \kappa$ is the change in curvature. For a full derivation of the stress to frequency equations, see Appendix C of the supplementary material. For a typical thin metal film (0–1 μm) on a QCM, the curvature measurement has an uncertainty of 0.001 m^{-1} which corresponds to a stress uncertainty of 0.006 MPa per micron of film thickness from this calculation.

An example of the contribution of stress to the total frequency change can be seen in Fig. 9. Here we use a 335 nm palladium film, which has a well-known hydrogen loading fraction to confirm the equations above. The gas pressure and composition of the chamber also contribute to the frequency change, and these effects are calibrated out using the measured frequency of the QCM on the secondary control stage caused solely by environmental effects. The frequency from the mass change of the sample can be calculated from the total frequency change using the following
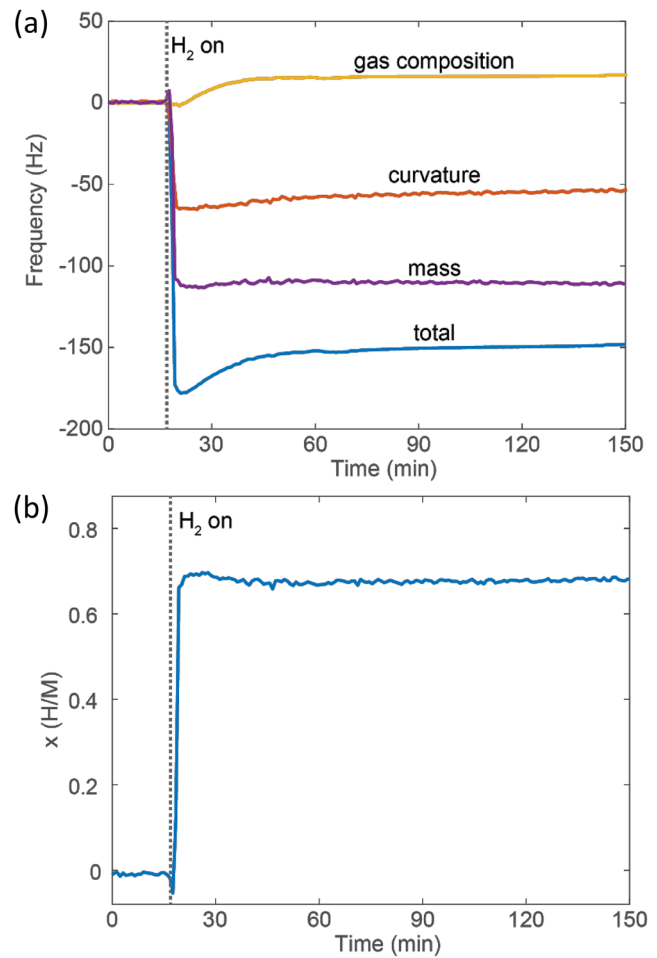

FIG. 9. (a) Plot of QCM frequency change during hydrogen loading of a 335 nm thick Pd film. The blue curve is the measured frequency of the active QCM, the yellow curve is the measured frequency of the secondary blank QCM, and the orange curve is the frequency contribution from the stress in the active QCM, as calculated from the curvature. By subtracting the stress and gas composition contributions from the total measured frequency, we obtain the frequency change due to the added mass of the hydrogen within the Pd lattice (purple curve). (b) Mass loading fraction X upon introduction of H$_2$.

equation:

$$\Delta f_m = \Delta f_{tot} - \Delta f_{gas} - \Delta f_\sigma$$
$$= \Delta f_{tot} - \Delta f_{secondary} - \alpha \Delta \kappa, \tag{2}$$

where Δf_m is the frequency change due to a mass change, Δf_{tot} is the total frequency change, Δf_{gas} is the frequency change due to environmental effects, Δf_σ is the frequency change due to stress, and $\Delta f_{secondary}$ is the measured frequency of the blank QCM on the secondary control stage. The mass-induced frequency change can then be converted to the hydrogen loading with the equation

$$\Delta x = \frac{\Delta f_m A_M}{\rho_M t_f A_H C_f}, \tag{3}$$

where Δx is the change in hydrogen atoms in the lattice per metal atom, A_i is the atomic mass of species i (either M, the metal host, or H, hydrogen), ρ_M is the density of the unloaded metal M, t_f is the film thickness, and C_f is the Sauerbrey coefficient from the literature relating a frequency change to a corresponding mass change. The uncertainty of the mass change measurement in our system is 13 ng/cm^2, which is dominated

by the uncertainty in curvature. It should be noted that the extra mass and varied impedance associated with RTDs, insulating layers, and the film under test result in a correction to the Sauerbrey coefficient of <2% (determined by full transmission line simulation as per Steinem and Janshoff;[10] see Appendix A for the layers of the RTD system). However, this correction factor lies within the uncertainty for a typical gas phase loading experiment and can generally be ignored. The measured loading fraction of 0.7 agrees with the well-known value for palladium at this pressure (9.3 bars).[23,24]

CALORIMETRY

We use a one-state nonlinear lumped element model to describe our system (i.e., the state is described by a single variable) with thermal potentials measured at discrete positions by our RTDs.[25] This model takes the difference of the normalized resistances of the outer and center RTDs as the independent variable (i.e., state variable of the single floating node), τ, which is a function of the differential temperature between the center and outside of the QCM. Thus, all that is needed is a measure of relative temperature during a system calibration, which may then be used to infer the input power (from any source) during an experiment. The thermal power input sources are the powers from the RTDs, P_{RTD}, the laser or laser induced reactions, P_{Laser}, the heat from running current through the sample thin film or thin film reactions, P_{Disk}, and the heat from running current through the central heating element, P_{Heater}. Figure 10 shows a schematic of the lumped element model with the thermal resistor and capacitor driven by the inputs and tied to a thermal ground. While only two RTDs are utilized in the one-state model, we have included a third RTD on the QCM. This third (midway) RTD presents an opportunity for a two-state model (using τ and a second state variable), which could offer higher precision as well as additional information about heat localization but would require more development and an extended calibration process. Thus, a two-state model is left as a future refinement.

This one-state system can be modelled with a first order differential equation described by a single independent state variable τ and is given by

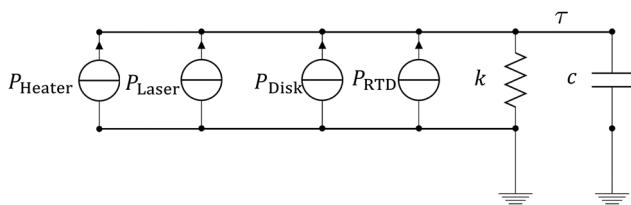$$P_{\text{In}}(t) = k\tau + C\frac{d\tau}{dt} \qquad (4)$$

FIG. 10. The four source, one-state lumped-element calorimetric model diagram. The four contributing powers measured into the sample are the input powers from the RTDs, P_{RTD}, the laser or laser induced reactions, P_{Laser}, the heat from running current through the sample thin film or thin film reactions, P_{Disk}, and the heat from running current through the central heating element, P_{Heater}. The state variable, τ, is the relative thermal gradient of the system defined by the difference between normalized (to equilibrium resistance) center and outer RTD resistances. k and C are the thermal conductance and thermal capacitance of the system, respectively.

with

$$\tau \equiv \frac{R_{\text{Center}}(t)}{R_{\text{Center},0}} - \frac{R_{\text{Outer}}(t)}{R_{\text{Outer},0}}. \qquad (5)$$

Here P_{In} is the total effective input power (i.e., the sum of the individual input powers weighted by power distribution scaling factors, see below), $R_i(t)$ is the measured resistance of RTD i at time t, and $R_{i,0}$ is the measured near-equilibrium resistance of RTD i (i.e., the resistance when the only input power to the system is the small RTD sensing current). The nonlinear thermal conductance, k, and capacitance, C, depend on the state variable and the partial gas pressures. These values are given by

$$k = k_0 + k_\tau \tau + \sum_{n=0}^{N} k_{\rho_n} \rho_n + k_{\rho_n,2\rho_n^2}, \qquad (6)$$

$$C = C_0 + \sum_{n=0}^{N} C_{\rho_n} \rho_n + C_{\rho_n,2\rho_n^2}, \qquad (7)$$

where ρ_n is the partial pressure of gas species n. Note that when the system is operated at a constant total pressure and with a mix of two gases, as is often the case, the partial pressure terms can be collapsed to a single term. With all the constants above known, the total input power may be inferred. However, these constants must first be determined during the calibration process (i.e., system identification), when known powers are input into the system and the constants are fit using Eq. (4). The effective total input power during the system identification process is given by

$$P_{\text{In}}(t) = P_{\text{RTDs}}(t) + P_{\text{Disk}}(t)\left(A_{\text{Disk}} + \sum_{n=0}^{N} A_{\text{Disk},\rho_n} \rho_n\right) \\ + P_{\text{Laser}}(t)A_{\text{Laser}}, \qquad (8)$$

where P_i and A_i and are, respectively, the input powers and the power distribution scaling factor of power type i, with $A_{i,\rho n}$ being the proportion due to the change in partial pressure n. These power distribution scaling factors are a result of the differences in the spatial distribution of the heat sources and are also fit during the calibration process. The terms that include partial pressures represent the differences in effective power due to the spatial distributions. As noted above in the case of a constant total pressure composed of two gases, the sum can collapse to a single term.

A complete calorimetry measurement of a sample is composed of three sections: experiment where we measure the heat of a reaction, calibration where we fit a system model, and prediction where we confirm the accuracy of the model. After each experimental section, a system identification cycle is run where various known power inputs are applied at higher powers and frequencies than expected in the experimental run. The results of these excitations are used to fit the parameters defined above (A's, k's, and C's). While this system identification step could theoretically be conducted before the experiment, it requires changing the reactive gas partial pressure, which in the case of irreversible gas-based reactions would cause the sample to be fully reacted before the experimental section. While the equations above present a comprehensive system, generally the calibration should be tailored to the experiment, which may allow for reduced dimensionality of the fit. The fitting

process uses Matlab System Identification Toolbox together with the freely available Calorimetry System Identification (CSID). This Matlab toolbox takes a set of user defined differential equations with unidentified constants (A's, k's, and C's) and uses a calibration dataset (known inputs with measured outputs) to fit these constants. The CSID adds additional functionality and gives examples specific to identification of calorimetric systems. See Appendix D of the supplementary material for more information on the typical calibration procedure used here. The quality of the fit is then tested with another set of more gentle excitations of the various power sources in a prediction run that immediately follows the calibration cycle. Data recorded from a typical prediction run are compared to the output of the calibrated model in Fig. 11. This run shows a normalized (by the mean value) root mean squared error between measured and modeled data of 8%. We also compare the energy calculated from the disk power in a single pulse to that of the energy modeled. This comparison gives the accuracy of the energy inferred from a potential chemical reaction on a similar time scale and power to that of the pulse, assuming that P_{Disk} is an analog to the power of the reaction. Here we define our metric as the difference between the integrated excess calculated power (difference between the quiescent power and pulse power) and integrated excess effective input power (P_{in}) divided by the integrated modelled power over the pulse region. In the run shown, we find this average error to be 4% for the short 65 mJ pulses and 2% for the larger 325 mJ pulses in 100% H_2. The improved accuracy compared to the error for the total run arises from

sensor drift. Finally, to put bounds on the instantaneous power accuracy and resolution of our system, we consider the sensor drift over the course of a 10 h experiment. The typical sensor drift on this time scale is 75 ppm which corresponds to 150 μW of apparent power drift. We address the causes and potential improvements to the calorimeter in the Appendix D of the supplementary material.

CONCLUSIONS

In this manuscript, we have presented a novel apparatus with the combined capability to measure stress, mass, and heat while pressurized under a reactive gas and retaining optical access to the sample. The incorporation of stress compensation allows for the accurate determination of mass loading. Prior studies on QCMs have neglected this important factor, likely resulting in anomalous mass determinations. We have demonstrated the ability of our chamber to hold pressure at 9.31 ± 0.02 bars of H_2 at 24.85 ± 0.05 °C with a leak rate of 2 SCCM. On a 335 nm thin film palladium sample, we demonstrated a measurement sensitivity of 0.001 m^{-1} of curvature, corresponding to a stress sensitivity of 0.006 MPa per micron of film thickness, and a mass measurement sensitivity of 13 ng/cm^2. Using a one state lumped-parameter heat transfer model, the heat creation of a reaction can be measured with 150 μW accuracy. The on-chip calorimetry scheme allows for a very flexible system where small heats can be detected in thin films, which might be overwhelmed by the base noise if the temperature measuring elements were located farther from the sample.

This instrument enables the study of phenomena including the ellipsometric determination of optical properties at varied metal hydride compositions, measurement of interfacial energies between metals and various substrates, spectroscopic measurement of nanoparticle resonance frequency for optical analysis of chemical processes or optical calorimetry, and the direct quantification of heat and stress from coupled plasmonic excitations. Many of these phenomena have not been thoroughly explored because of the inability to collect all of the necessary data simultaneously throughout a reaction. The combination of these measurements will lead to new insights in nanoscale reactions. Furthermore, the integration of optical access with the other capabilities already described offers interesting possibilities for expanding the scope of this apparatus.

SUPPLEMENTARY MATERIAL

See supplementary material for details on sample fabrication and characterization (Appendix A), gas thermal conductivity and control (Appendix B), curvature calculations (Appendix C), and calorimetry setup and calibration (Appendix D).
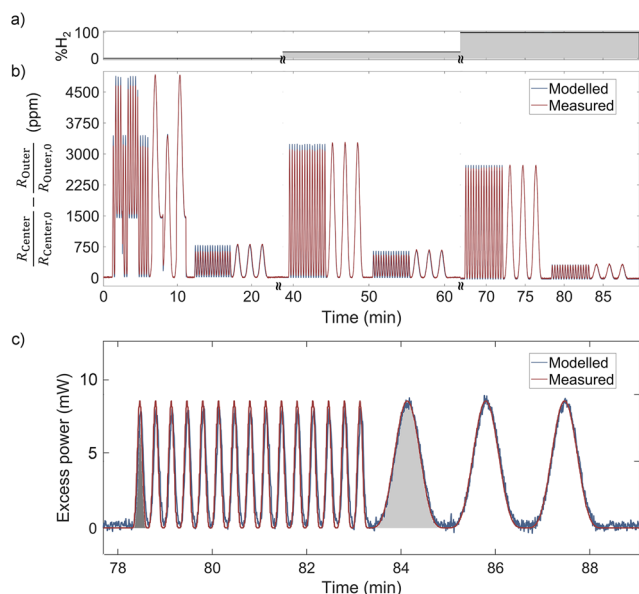
FIG. 11. Modeled and measured calorimetry data for a thin Cr film during the prediction portion of a run in which the accuracy of the calibration is assessed. (a) Calculated H_2 partial pressure of the system. (b) The system is excited with each of the power sources. The red line is the state variable measured by the apparatus, and the blue line is the output of the model of these data. (c) Modelled and measured excess powers due to pulses of the disk heating power during the final portion of the prediction section. The system is thermally excited by flowing current through the film. This portion corresponds to the integration region used to calculate the accuracies of the energy pulses. Here the integration is represented by the shaded areas with dark grey for the short 65 mJ pulses and light grey for the larger 325 mJ pulses.

[1] M. S. Wilson and S. Gottesfeld, J. Appl. Electrochem. **22**, 1 (1992).

[2] J. Kibsgaard, Z. Chen, B. N. Reinecke, and T. F. Jaramillo, Nat. Mater. **11**, 963 (2012).

[3] P. Strasser, S. Koh, T. Anniyev, J. Greeley, K. More, C. Yu, Z. Liu, S. Kaya, D. Nordlund, H. Ogasawara, M. F. Toney, and A. Nilsson, Nat. Chem. **2**, 454 (2010).

[4] J. B. Bates, N. J. Dudney, B. Neudecker, A. Ueda, and C. D. Evans, Solid State Ionics **135**, 33 (2000).

[5] N. Liu, H. Wu, M. T. McDowell, Y. Yao, C. Wang, and Y. Cui, Nano Lett. **12**, 3315 (2012).

[6] M. S. Gudiksen, L. J. Lauhon, J. Wang, D. C. Smith, and C. M. Lieber, Nature **415**, 617 (2002).

[7] K. Nomura, H. Ohta, K. Ueda, T. Kamiya, M. Hirano, and H. Hosono, Science **300**, 1269 (2003).

[8] A. N. Shipway, E. Katz, and I. Willner, ChemPhysChem **1**, 18 (2000).

[9] G. Sauerbrey, Z. Phys. **155**, 206 (1959).

[10] *Piezoelectric Sensors*, edited by C. Steinem and A. Janshoff (Springer-Verlag, Berlin, Heidelberg, 2007).

[11] I. Reviakine, D. Johannsmann, and R. P. Richter, Anal. Chem. **83**, 8838 (2011).

[12] A. P. M. Glassford, J. Vac. Sci. Technol. **15**, 1836 (1978).

[13] K. K. Kanazawa and J. G. Gordon, Anal. Chem. **57**, 1770 (1985).

[14] K. Keiji Kanazawa and J. G. Gordon, Anal. Chim. Acta **175**, 99 (1985).

[15] E. P. EerNisse, J. Appl. Phys. **43**, 1330 (1972).

[16] E. P. EerNisse, J. Appl. Phys. **44**, 4482 (1973).

[17] T. P. Leervad Pedersen, C. Liesch, C. Salinga, T. Eleftheriadis, H. Weis, and M. Wuttig, Thin Solid Films **458**, 299 (2004).

[18] V. A. Sethuraman, M. J. Chon, M. Shimshak, V. Srinivasan, and P. R. Guduru, J. Power Sources **195**, 5062 (2010).

[19] M. Schwind, S. Hosseinpour, C. Langhammer, I. Zorić, C. Leygraf, and B. Kasemo, J. Electrochem. Soc. **160**, C487 (2013).

[20] M. Schwind, C. Langhammer, B. Kasemo, and I. Zorić, Appl. Surf. Sci. **257**, 5679 (2011).

[21] A. L. Smith and H. M. Shirazi, Thermochim. Acta **432**, 202 (2005).

[22] C. Langhammer, E. M. Larsson, B. Kasemo, and I. Zorić, Nano Lett. **10**, 3529 (2010).

[23] R. V. Bucur, V. Mecea, and T. B. Flanagan, Surf. Sci. **54**, 477 (1976).

[24] R. Feenstra, D. G. de Groot, J. H. Rector, E. Salomons, and R. Griessen, J. Phys. F: Met. Phys. **16**, 1953 (1986).

[25] G. Sidebotham, *Heat Transfer Modeling: An Inductive Approach* (Springer International Publishing, 2015).